

See discussions, stats, and author profiles for this publication at: <https://www.researchgate.net/publication/7736920>

# Backbone Dynamics of the Olfactory Marker Protein As Studied by 15 N NMR Relaxation Measurements †

ARTICLE *in* BIOCHEMISTRY · AUGUST 2005

Impact Factor: 3.02 · DOI: 10.1021/bi050149t · Source: PubMed

CITATIONS

11

READS

12

6 AUTHORS, INCLUDING:



**Nathan T Wright**

James Madison University

32 PUBLICATIONS 543 CITATIONS

SEE PROFILE



**Kristen M Varney**

University of Maryland, Baltimore

36 PUBLICATIONS 891 CITATIONS

SEE PROFILE



**David Joseph Weber**

University of Maryland, Baltimore

126 PUBLICATIONS 3,832 CITATIONS

SEE PROFILE

# Backbone Dynamics of the Olfactory Marker Protein As Studied by $^{15}\text{N}$ NMR Relaxation Measurements<sup>†</sup>

Rossitza K. Gitti,<sup>‡</sup> Nathan T. Wright,<sup>‡</sup> Joyce W. Margolis,<sup>§</sup> Kristen M. Varney,<sup>‡</sup> David J. Weber,<sup>\*,‡</sup> and Frank L. Margolis<sup>\*,§</sup>

Department of Biochemistry and Molecular Biology, University of Maryland School of Medicine, 108 North Greene Street, Baltimore, Maryland 21201, and Department of Anatomy and Neurobiology, University of Maryland School of Medicine, 20 Penn Street, Baltimore, Maryland 21201

Received January 26, 2005; Revised Manuscript Received May 16, 2005

**ABSTRACT:** Nuclear magnetic resonance (NMR)  $^{15}\text{N}$  relaxation measurements of the olfactory marker protein (OMP) including longitudinal relaxation ( $T_1$ ), transverse relaxation ( $T_2$ ), and  $^{15}\text{N}$ – $\{^1\text{H}\}$  NOE data were collected at low protein concentrations ( $\leq 100 \mu\text{M}$ ) and at two field strengths (14.4 and 18.8 T) for 135 of 162 backbone amide groups. Rotational diffusion of the OMP was found to be axially symmetric with  $D_{\parallel}/D_{\perp} = 1.20 \pm 0.02$  with an overall global correlation time of  $8.93 \pm 0.03$  ns. Model-free internal dynamic analyses of these data provided a description of the protein's dynamics on multiple time scales. The results of these studies indicate that there is a large degree of conformational flexibility for  $\alpha$ -helix 1 ( $\alpha 1$ ), loop 1, and the conserved  $\Omega$ -loop (loop 3). The functional significance that these dynamic regions of OMP have in modulating olfactory signal transduction is discussed.

Olfactory marker protein (OMP)<sup>1</sup> expression is a hallmark of mature olfactory sensory neurons (1, 2). OMP is an abundant 19 kDa protein whose expression in these neurons is developmentally regulated and whose sequence is phylogenetically conserved in all vertebrates from fish to humans (1, 2). Evidence for its functional role in olfactory transduction derives from studies of OMP-KO mice in which the OMP gene was deleted by homologous recombination (3). These mice exhibit behavioral (4, 5) and electrophysiological (3, 6, 7) deficits in olfactory function that can be rescued by replacement of the OMP in olfactory sensory neurons using an adenoviral OMP expression vector (6, 8). In addition, recent studies demonstrate an alteration in the ability of these sensory neurons in the OMP-KO mice to regulate  $\text{Ca}^{2+}$  flux in response to ligand stimulation (9). These studies demonstrate a significant role for OMP in olfactory transduction and suggest its involvement in protein–protein interaction(s). Subsequent studies have confirmed this and demonstrated the interaction of OMP with members of the Bex protein family (10–12). Therefore, it was of interest to know the structural and dynamic characteristics of OMP as a first step in understanding the details of this protein–protein interaction.

Structures of rat OMP, determined by multidimensional NMR spectroscopy, and of mouse OMP, determined by X-ray crystallography at 2.3 Å resolution, have been reported (11, 13). The superposition of the two structures indicates a very similar  $\beta$ -clam fold with an RMSD of 2.13 Å for the  $\text{C}^{\alpha}$  atoms of residues in the  $\beta$ -sheets. However, only a few very weak long-range NOE constraints were available for the first helix of OMP ( $\alpha 1$ ) from the NMR data, and  $T_2$  broadening has been observed for several resonances in this helix (11). Therefore, the location of  $\alpha 1$  is not well-defined in the NMR solution structure. It is also possible that slow conformational exchange exists for  $\alpha 1$  and that this helix and other regions of OMP are dynamic in solution, which is the focus of this NMR  $^{15}\text{N}$  relaxation study. In this paper, the dynamic properties of  $\alpha 1$ , loop 1, and the  $\Omega$  loop (loop 3) of OMP indicate that these three regions of OMP are all dynamic in solution on multiple time scales.

## MATERIALS AND METHODS

**Sample Preparation.**  $^{15}\text{N}$ -Labeled recombinant rat OMP was generated and purified as described previously (11). NMR samples used for  $^{15}\text{N}$  relaxation rate studies were 0.05–0.10 mM OMP in 95%:5%  $\text{H}_2\text{O}$ : $\text{D}_2\text{O}$  containing 5.0 mM  $\text{Na}_2\text{HPO}_4$  (pH = 6.6), 0.3 mM  $\text{NaN}_3$ , and 0.1 mM  $\text{Na}_2\text{EDTA}$ . Samples with protein concentrations higher than 0.1 mM resulted in faster  $R_2$  rates in a concentration-dependent manner consistent with OMP self-association, so only protein samples at concentrations of 0.1 mM or less were used in the final analyses. All solutions used to prepare the NMR sample were filter-sterilized (0.2  $\mu\text{m}$  pore size) and deoxygenated by purging with helium for 10 min.

For aligned samples, necessary to collect residual dipolar coupling data, OMP was prepared in radially compressed (stretched) polyacrylamide gels as previously described (14,

<sup>†</sup> This work was supported by NIH Grants GM58888 (D.J.W.), DC04752 (R.K.G.), and DC03112 (F.L.M.).

\* Corresponding authors. F.L.M.: e-mail, fmargoli@umaryland.edu; telephone, (410) 706-8913. D.J.W.: e-mail, dweber@umaryland.edu; telephone, (410) 706-4354.

<sup>‡</sup> Department of Biochemistry and Molecular Biology, University of Maryland School of Medicine.

<sup>§</sup> Department of Anatomy and Neurobiology, University of Maryland School of Medicine.

<sup>1</sup> Abbreviations: OMP, olfactory marker protein; KO, knock out; ppm, parts per million; NMR, nuclear magnetic resonance; NOE, nuclear Overhauser effect; PDB, Protein Data Bank; RMS, root mean square; CSA, chemical shift anisotropy.

15). Briefly, polyacrylamide gels were prepared to a final polyacrylamide concentration of 5.5% and cast in a gel stretcher apparatus (New Era Enterprises, Inc.) (14). After the gel was allowed to polymerize, it was washed in doubly distilled deionized water for 1 h ( $\times 3$ ) and soaked in the NMR buffer described above without OMP. The gel was then cut to 10 mm and soaked overnight in 400  $\mu$ L of 0.5 mM OMP in the above NMR buffer plus 20% D<sub>2</sub>O and 0.4 mM sodium azide. The next day, the gel was placed into a stretching apparatus and forced through a funnel and into an open-ended 5 mm NMR tube, which results in stretching the gel from 10 to 20 mm in length by radial compression. The bottom of the tube was sealed, a plunger was placed on the top of the tube, and the tube was sealed with a cap and Parafilm prior to data collection.

**NMR Data Collection.** Nuclear magnetic resonance <sup>15</sup>N T<sub>1</sub>, T<sub>2</sub>, and <sup>15</sup>N-<sup>1</sup>H NOE experiments were carried out at 37 °C using Bruker DMX 600 MHz and Bruker Avance 800 MHz NMR instruments, both equipped with z-axis gradient cryogenic probes. A 2D IPAP <sup>1</sup>H-<sup>15</sup>N HSQC was also collected on isotopic and aligned OMP samples as previously described (16). For all experiments, the <sup>1</sup>H carrier was set on the water frequency, and the <sup>15</sup>N carrier frequency was at 118.6 ppm. Water flip-back (17) and field gradient pulses (18) were used to suppress the water signal without saturation. NMR <sup>15</sup>N T<sub>1</sub> measurements were recorded with spectral widths 12.5 ppm (<sup>1</sup>H, F<sub>2</sub>) and 27 ppm (<sup>15</sup>N, F<sub>1</sub>), and data (192  $\times$  1024 complex matrices) were acquired for seven durations of the T<sub>1</sub> relaxation delay: T = 10 ( $\times 2$ ), 50, 100, 400, 1000 ( $\times 2$ ), 1600, and 2100 ms. The <sup>15</sup>N T<sub>2</sub> measurements were collected with fully interleaved planes (19, 20) and a 180 deg pulse-repetition rate in the CPMG pulse train of 0.9 ms. The same spectral widths and data size matrices were used as for the <sup>15</sup>N T<sub>1</sub> experiments for seven <sup>15</sup>N T<sub>2</sub> relaxation delays: T = 12 ( $\times 2$ ), 24, 36, 60, 96 ( $\times 2$ ), 120, and 144 ms. The T<sub>1</sub> and T<sub>2</sub> measurements of decay data were fit with a two-parameter exponential decay as previously described (21). All data were collected with 32 and 64 scans per increment on the 800 and 600 MHz NMR spectrometers, respectively. A 1.8 s relaxation delay was used between scans for both T<sub>1</sub> and T<sub>2</sub> measurements. The <sup>15</sup>N-<sup>1</sup>H NOE spectra were recorded with proton saturation using a 3.0 s pre-delay followed by a 3 s period of saturation and interleaved with the reference spectrum, which was recorded with 6 s pre-delay and no saturation. The flip-back pulse sequence is used for measurement of the <sup>15</sup>N-<sup>1</sup>H NOE to return water magnetization to the +z-axis at the end of the each scan and to minimize effects of slowly relaxing water magnetization on the NOE measured for amides with rapidly exchanging protons, as previously described (17).

**T<sub>1</sub>, T<sub>2</sub>, and <sup>15</sup>N-<sup>1</sup>H NOE Relaxation Data Analysis.** The relaxation data sets were processed with 63°-shifted square sine-bell filtering in both dimensions or Lorentzian-to-Gaussian apodization functions for the lower intensity contours and zero filling to 512  $\times$  2048 data points using the program NMRPipe (22), and resonance intensities at various relaxation delays were determined using the NMR-View software package (23). The <sup>15</sup>N R<sub>1</sub> and R<sub>2</sub> relaxation rates were obtained by fitting the cross-peak intensities as a function of relaxation delay time to a two-parameter exponential decay function using the Levenberg-Marquardt

nonlinear least-squares fitting program Curvefit (A. G. Palmer III, Columbia University), and uncertainties in the fitted parameters were estimated using Jackknife simulations (A. G. Palmer III, Columbia University). Experimental errors associated with R<sub>1</sub> and R<sub>2</sub> relaxation rates were estimated from peak intensities for duplicate data sets collected with the same relaxation delays and the root-mean-square deviation in noise (24, 25). The average percentage deviation for the T<sub>1</sub> and T<sub>2</sub> data was 3.5% and 5%, respectively.

The NOE enhancement was calculated as a ratio between the cross-peak intensities with (I) and without (I<sub>0</sub>) <sup>1</sup>H saturation. Minimal or no correction of the measured NOE enhancements (NOE<sub>m</sub>) for incomplete magnetization recovery during the 3.0 s repetition delay was necessary. To obtain reliable error estimates for the NOE measurements at the relatively low experimental protein concentrations used in this study, three pairs of NOE data sets (with and without <sup>1</sup>H saturation for each pair) were performed. The errors in the NOE values were obtained by comparing the reproducibility of intensity values, and the uncertainties in the peak heights were assumed to equal the RMS noise in each of the corresponding spectra as previously described (25, 26). The average percentage error for the NOE was 6% in the three data sets. Knowledge of the rotational diffusion tensor is necessary for a detailed analysis of the dynamics of nonspherical proteins. For isotropic rotational motion,  $\tau_m$  is direction independent and is given by the expression

$$(6\tau_m)^{-1} = D_{\text{iso}} \quad (1)$$

where  $D_{\text{iso}} = \text{Tr}\{\mathbf{D}\}/3 = (D_{xx} + D_{yy} + D_{zz})/3$  and thus contains no structural information. An expression relating the spectral density function  $J(\omega)$  to the anisotropic diffusion tensor,  $\mathbf{D}$ , was given by Woessner (27). In the case of anisotropic rotational diffusion, the dependence of  $\tau_m$  on the direction of the NH vectors relative to the principal axes of the diffusion tensor is given by

$$(6\tau_{m,i})^{-1} = \mathbf{e}_i^T \mathbf{D} \mathbf{e}_i \quad (2)$$

where  $\mathbf{e}_i = (x_i, y_i, z_i)$  is the normalized interatomic vector of the <sup>15</sup>N-<sup>1</sup>H pair *i*. Specifically,  $x_i$ ,  $y_i$ , and  $z_i$  are the direction cosines defining the orientation of the *i*th NH bond vector in the principal axes frame of the diffusion tensor (27, 28). The anisotropic diffusion tensor,  $\mathbf{D}$ , is defined by six parameters that are the rotational diffusion constants along the three principal axes  $D_{xx}$ ,  $D_{yy}$ , and  $D_{zz}$  and the Euler angles  $\alpha$ ,  $\beta$ , and  $\gamma$  which determine the orientation of the diffusion frame with respect to a molecular fixed reference frame. For an axially symmetric diffusion tensor with components  $D_{zz} = D_{\parallel}$  and  $D_{xx} = D_{yy} = D_{\perp}$ , four parameters are optimized to describe the orientation and the amplitude of its principal component ( $D_{\parallel}$ ,  $D_{\perp}$ ,  $\theta$ , and  $\phi$ ).

Both the principal components and the orientation of the diffusion tensor of a protein can be reliably determined from the angular dependence of the relaxation rates of a subset of NH vectors assumed to have a negligible component of internal motions and/or exchange contributions to the <sup>15</sup>N relaxation. For this subset of residues, the R<sub>2</sub>/R<sub>1</sub> ratio is dependent only on the overall tumbling component of the spectral density function  $J(\omega)$  and can be used to calculate the global molecular correlation time. In general, the selection

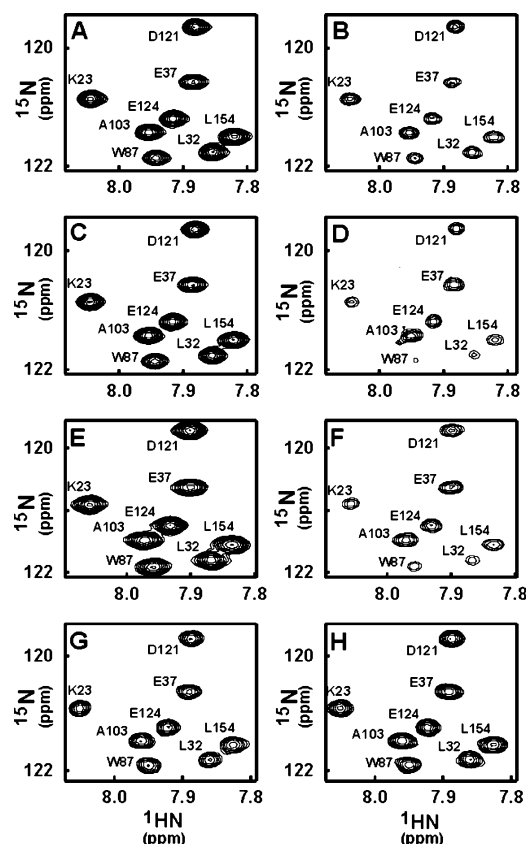


FIGURE 1: Representative  $T_1$ ,  $T_2$ , and heteronuclear NOE  $^{15}\text{N}$  relaxation rate data for OMP. (A, B) Shown are  $T_1$  data at 800 MHz for the shortest relaxation delay (A,  $\tau = 0.010$  s) and longest delay (B,  $\tau = 2.10$  s). (C, D) Shown are representative  $T_2$  data at 800 MHz for planes with the shortest (C,  $\tau = 0.012$  s) and longest (D,  $\tau = 0.120$  s) relaxation delays. (E, F) Representative  $T_2$  data at 600 MHz are illustrated for planes with the shortest (E,  $\tau = 0.012$  s) and longest (F,  $\tau = 0.120$  s) relaxation delays. (G, H) A region of the  $^{15}\text{N}$  heteronuclear NOE spectra at 800 MHz is illustrated (G) with saturation and (H) without saturation. The number of scans is 64 and 32 at 61 and 81 MHz, respectively. The sample contained 0.1 mM OMP, 5%  $\text{H}_2\text{O}$ , 5.0 mM  $\text{Na}_2\text{HPO}_4$ , 0.3 mM  $\text{NaN}_3$ , and 0.1 mM NaEDTA, pH 6.6, 37 °C.

of a subset of rigid vectors can be accomplished by subjecting residues with  $\text{NOE} > 0.65$  to the exclusion criteria given as

$$\text{NOE} < \text{NOE}_{\text{av}} - 1.5\text{SD} \quad (3)$$

and

$$\{(\langle T_2 \rangle - T_{2,n})/\langle T_2 \rangle\} - \{(\langle T_1 \rangle - T_{1,n})/\langle T_1 \rangle\} > 1.5\text{SD} \quad (4)$$

where SD is the standard deviation of the function for residue “n” (29, 30). For helix 1 and other smaller stretches, when several consecutive residues did not meet these criteria, the entire region was excluded from the diffusion tensor calculations (31, 32).

## RESULTS

**NMR  $^{15}\text{N}$  Relaxation and Backbone Dynamics.** There are seven proline residues and six residues with nondetectable  $^1\text{H}$ – $^{15}\text{N}$  correlations (M1, A2, G42, Q61, Q85, and N93), due most likely to exchange broadening (11). This leaves 150 out of 163 residues with observable H–N correlations in the OMP samples (Figure 1). Excluding residues with

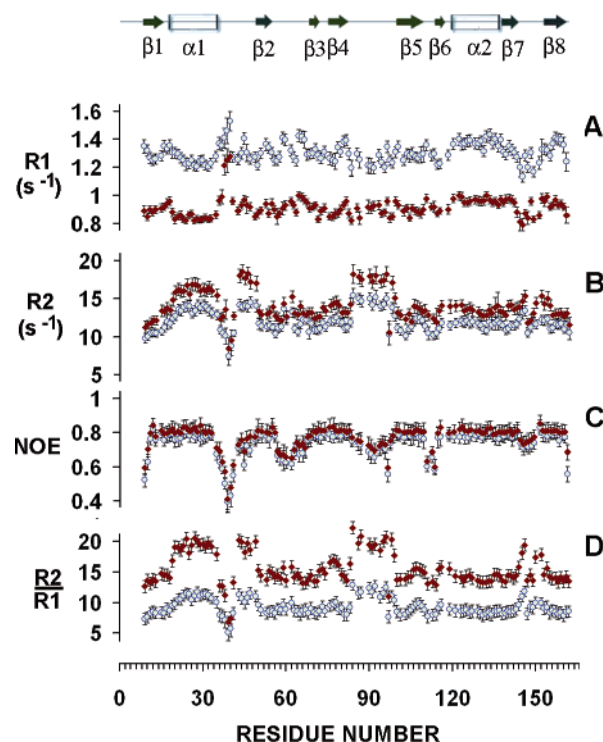


FIGURE 2: OMP  $^{15}\text{N}$  relaxation rate data at 61 MHz (gray circles) and 81 MHz (red diamonds) plotted as a function of residue number. Shown are (A)  $R_1$  data, (B)  $R_2$  data, (C) heteronuclear NOE data, and (D)  $R_2/R_1$  ratios for each residue. The secondary structure of OMP is also illustrated above the data for each residue.

overlapping or very weak correlation peaks, a total of 135 residues were used for the relaxation analysis.  $R_1$  and  $R_2$  relaxation rates were acquired at seven different protein concentrations: 0.05, 0.10, 0.20, 0.50, 0.65, 1.0, and 1.85 mM. At the higher protein concentrations (0.50–1.85 mM), a small protein concentration dependence in  $R_2$  was observed, indicative of minimal contributions to relaxation from self-association (data not shown). Fortunately,  $^{15}\text{N}$  NOE,  $R_1$ , and  $R_2$  relaxation rates were unchanged from 0.05 to 0.2 mM OMP, indicating that the protein is not self-associating under these experimental conditions. Therefore, only data collected with 0.1 mM OMP concentration or less were used in the final analyses (Figure 1). The  $^{15}\text{N}$  longitudinal relaxation rate ( $R_1$ ),  $^{15}\text{N}$  spin–spin relaxation rate ( $R_2$ ), the  $R_2/R_1$  ratio, and the  $^{15}\text{N}$ – $\{^1\text{H}\}$  NOE versus residue number are presented in Figure 2.

The structure of OMP consists of a  $\beta$ -sheet in the form of a  $\beta$ -clam ( $\beta 1$ , residues Q10–D18;  $\beta 2$ , residues E50–D56;  $\beta 3$ , residues N69–D73;  $\beta 4$ , residues G76–T83;  $\beta 5$ , residues L100–K109;  $\beta 6$ , residues A114–N118;  $\beta 7$ , residues V138–T144;  $\beta 8$ , residues N153–Q162), two  $\alpha$ -helices ( $\alpha 1$ , residues D20–Q34;  $\alpha 2$ , residues A120–K134), and four loops (loop 1, residues R35–A49; loop 2, residues F57–W68;  $\Omega$  loop 3, S84–L99;  $\beta$ -hairpin loop 4, F145–A152) (11, 13). Residues of the  $\beta$ -clam core of the protein ( $\beta 1$ – $\beta 8$ ) and the  $\alpha 2$  helix exhibit low mobility on fast time scales as judged by high average  $^{15}\text{N}$ – $\{^1\text{H}\}$  NOE values ( $^{\text{av}}$ NOE values of 0.78 and 0.81 at 61 and 81 MHz, respectively) and represent a relatively rigid and compact region of the protein structure; this is consistent with the previously observed slow NH exchange rates (11).

However, the  $\alpha 1$  helix shows different relaxation behavior compared to the structural core of the protein. Although the



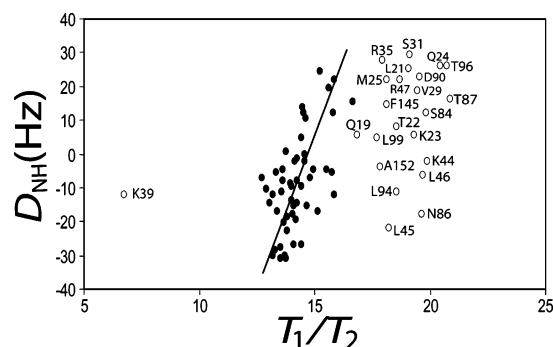


FIGURE 3: Plot of  $^{15}\text{N}$   $T_1/T_2$  ratios (61 MHz) versus residual dipolar coupling values ( $^1D_{\text{NH}}$ ) for residues of OMP. Data included in the linear correlation are displayed as filled circles (●) and the outliers as open circles (○).

average NOE of 0.8 (0.78 and 0.81 at 61 and 81 MHz, respectively) for the residues in this helix (Figure 2) is indicative of low-amplitude motions on fast time scales, the higher than average  $R_2$  rates and the  $R_2/R_1$  ratio for helix 1 ( $R_2/R_1$  at 61 MHz of 11.0;  $R_2/R_1$  at 81 MHz of 19.4) reveal a degree of conformational flexibility on slower time scales as compared to regions of the protein with little or no  $T_2$  broadening ( $R_2/R_1$  at 61 MHz of 8.6;  $R_1/R_2$  at 81 MHz of 14.5; Figure 2). That these residues have  $R_{\text{ex}}$  contributions to  $T_2$  relaxation is further supported in a plot of residual dipolar couplings ( $^1D_{\text{NH}}$ ) versus  $T_1/T_2$  (33) (Figure 3), which identified 7 of 14 residues in this helix (L21, T22, K23, Q24, M25, V29, and S31) as having conformational exchange. Such exchange broadening effects observed in helix 1 are most likely the reason why very few long-range NOESY correlations and fast amide-proton exchanges were observed from residues in this helix (11).

The disorder of the loop regions of OMP (loop 1, R35–A49; loop 2, F57–W68; and  $\Omega$  loop 3, S84–L99) is reflected in the observed low NOE values, which are characteristic for fast frequency component contributions to the relaxation of these residues. Additionally, several residues in all three loops have fast  $R_2$  relaxation rates or are missing altogether, including residues in loop 1 (E43–A49), the majority of residues in the  $\Omega$  loop (loop 3; residues 84–99), and three residues in the  $\beta$ -hairpin loop (loop 4; residues F145, G146, E150). These effects are indicative of low frequency component contributions to the relaxation and are characteristic of conformational exchange on the millisecond time scale (i.e.,  $R_{\text{ex}}$ ). As found for helix 1, residues in loop 1 (R35, K39, L44, L45, L46, R47) and loop 3 (S84, N86, T87, D90, L94, T96, L99) were confirmed to have exchange contributions to  $T_2$  relaxation in a plot of  $^1D_{\text{NH}}$  versus  $T_1/T_2$  ratio (Figure 3). Both loop 1 and  $\Omega$  loop 3 are considerably long, allowing for a large degree of conformational flexibility for these regions of the protein. It is possible that the very large decrease in  $^{15}\text{N}$ – $\{^1\text{H}\}$  NOE values ( $<0.6$ ) just after helix 1, in loop 1, may be identifying residues of OMP that serve as a “hinge” that allows regions of this loop and helix 1 to sample multiple conformations in solution on slower time scales. For  $\Omega$  loop 3, decrease in  $^{15}\text{N}$ – $\{^1\text{H}\}$  NOE is less pronounced than that in loop 1 ( $<0.8$ ), but it also is quite mobile on slower time scales as judged by  $R_2/R_1$  ratios at both 61 and 81 MHz. As reflected by low NOE values (Figure 2), residues of the type I  $\beta$ -turn, which connects the antiparallel  $\beta$ -strands 5 and 6, exhibit an enhanced degree

of mobility on a fast time scale. As is often the case for proteins, residues at the amino and the carboxy termini, including loop 4, are also mobile on multiple time scales. Overall, the  $^{15}\text{N}$  relaxation rate data indicate that the OMP backbone dynamics occur over a wide range of time scales, including fast (picosecond to nanosecond) and slow (millisecond) internal motions (Figure 2).

**Rotational Diffusion Tensor Calculations for OMP.** Rotational diffusion parameters were determined by minimizing the difference between the experimental and calculated  $R_2/R_1$  ratios using isotropic, axially symmetric, and fully anisotropic diffusion models. A diffusion model was rejected, using the 95% confidence limit, if the experimental  $\chi^2$  was higher than the simulated  $\chi^2$  values from Monte Carlo sampling of Gaussian distributions based on the optimized parameters and the experimental errors. Excluding the higher  $R_2/R_1$  ratios observed for residues in the  $\alpha 1$  helix (average  $R_2/R_1$  at 61 MHz of 11.0;  $R_2/R_1$  at 81 MHz of 19.4), which are attributed to line broadening due to conformational exchange, the average values of the  $R_2/R_1$  ratios for helix  $\alpha 2$  and the eight  $\beta$ -strands at 61 MHz are 8.4 and 8.72 and at 81 MHz are 13.8 and 14.52, respectively. The components of the diffusion tensor were obtained using the program Quadric Diffusion (A. G. Palmer III, Columbia University) using a subset of  $R_2/R_1$  ratios from 62 residues from the  $\alpha 2$  helix and eight  $\beta$ -strands; unlike residues in the  $\alpha 1$  helix, these 62 residues did not exhibit conformational exchange using criteria described in Materials and Methods. The orientation of the components of the diffusion tensor calculated from 300 Monte Carlo simulations is consistent with the OMP having some rotational anisotropy. Under the assumption of isotropic motion, a global correlation time,  $\tau_m$ , of  $8.89 \pm 0.03$  ns was obtained using both the NMR and the crystal coordinates. Prior to this calculation, the NMR structure reported previously (11) was refined using the residual dipolar coupling constraints ( $^1D_{\text{NH}}$ ) to give a very good quality factor ( $Q = 0.19$ ; unpublished results), which was slightly better than that of the X-ray structure ( $Q = 0.28$ ). Considering the relatively large  $\chi^2$  ( $\chi^2_{\text{red}} = 1.37$ ), however, the isotropic model is in poor agreement with the relaxation data and is evidence of anisotropic tumbling. The fits of the NMR data to the axially symmetric tensor ( $\chi^2_{\text{red}} = 0.57$ ) and the fully anisotropic tensor ( $\chi^2_{\text{red}} = 0.58$ ) significantly improved the fits, but the two models could not be statistically distinguished using an  $F$ -test and the internal motion values assuming either axially symmetric or fully anisotropic models of motion were nearly identical (data not shown). Therefore, the simpler axially symmetric model was used to define the diffusion tensor, giving  $\tau_m = 8.93 \pm 0.03$  ns and  $D_{\parallel}/D_{\perp} = 1.20 \pm 0.02$ . The ratio of 1.00:0.86:0.45 for the principle components of the inertia tensor for the refined NMR structure is also consistent with the presence of anisotropic rotational diffusion; the  $z$ -axis of the inertia tensor ( $I_z$ ) and the diffusion tensor ( $D_z$ ) differs by  $15^\circ$  in both the NMR and X-ray structures. While differences in the inertia tensor ( $I_z$ ) and diffusion tensor ( $D_z$ ) such as these are not typical of most compact globular proteins, it is not too surprising a result for OMP because of the dynamic character of this protein, particularly involving helix 1 and loops 1 and 3, all of which are not accounted for in the inertia tensor calculation.

**Internal Motion Calculations for OMP.** The parameters of the internal motion for a total of 135 residues in OMP were optimized using an axially symmetric diffusion model with the program FAST-Modelfree (34). The confidence levels in the various models are estimated by Monte Carlo sampling methods in combination with appropriate  $\chi^2$  and  $F$ -tests. The backbone dynamic calculations for OMP were performed with 300 Monte Carlo simulations per run, assuming an internuclear distance,  $r_{\text{NH}}$ , of 1.02 Å and a chemical shift anisotropy of the  $^{15}\text{N}$  nucleus ( $\sigma_{\parallel} - \sigma_{\perp}$ ) of  $-160$  ppm. No significant differences in the calculated internal motion parameters were observed when using  $-170$  versus  $-160$  ppm for the chemical shift anisotropy (CSA) for the  $^{15}\text{N}$  nuclei. Five models of motion,  $M_i$ , were iteratively tested in order of increasing complexity ( $M_1, S^2$ ;  $M_2, S^2$ ,  $\tau_e = \tau_i$ ;  $M_3, S^2, R_{\text{ex}}$ ;  $M_4, S^2, \tau_e = \tau_i, R_{\text{ex}}$ ; and  $M_5, S^2, \tau_e = \tau_i, S^2, \tau_e = \tau_i$ ) until the tested model could reproduce the experimental relaxation data within 95% confidence limits, as described previously (35, 36). The use of three-parameter models for residues that exhibit  $R_{\text{ex}}$  (i.e., models 3 and 4) could be considered more rigorously since the relaxation rate data were collected at two field strengths (34). The calculations were performed using the relaxation rates and their uncertainties and the coordinates of the refined NMR or the X-ray structure as input (Figure 2; Tables 1s and 2s in Supporting Information).

Relaxation rate data for all of the residues were reasonably fit to a single model, and no residues were assigned to model 5 ( $M_5$ ) when using the NMR structure as input. Seventy-two residues, mainly present in the secondary structure elements (except from helix  $\alpha 1$ ), were assigned to  $M_1$ , with the average  $S^2 = 0.88 \pm 0.02$ . The relaxation of all residues of  $\alpha 1$  was best described with  $M_3$ , with average  $S^2 = 0.83 \pm 0.02$  and average  $R_{\text{ex}} = 2.4 \pm 0.3 \text{ s}^{-1}$  (61 MHz). Motion on the fast time scale was added to describe the internal motion of residues in the amino-terminal Q9–Q10; loop 1, R35–D41; loop 2, F57–H67; and residue Q162. Conformational exchange on the millisecond time scale,  $R_{\text{ex}}$ , and fast internal motions on the nanosecond to picosecond time scales characterize the dynamics of residues in loop 1 and the  $\Omega$  loop (Figure 3; Table 2s, 61 MHz). This result could be explained most simply by a single motion involving helix 1 and/or loop 1, which also displays exchange dynamics. When the analyses were repeated, using the crystal structure coordinates as input, the majority of the internal motion parameters of OMP were reproduced adequately, utilizing a slightly lower quality of fit ( $\chi_{\text{exp}}^2$  was higher), leaving eight residues that could not be assigned to a model (Table 2s).

## DISCUSSION

The concentration dependence of the experimental  $R_2$  rates shows clearly the tendency of OMP to self-associate at higher protein concentrations ( $>0.1 \text{ mM}$ ). Specifically, using  $R_2/R_1$  experimental ratios, the estimated molecular correlation times of  $13.26 \pm 0.04$ ,  $10.93 \pm 0.04$ ,  $10.21 \pm 0.3$ ,  $10.12 \pm 0.03$ ,  $9.23 \pm 0.03$ ,  $8.90 \pm 0.03$ , and  $9.01 \pm 0.08 \text{ ns}$  were calculated for relaxation rate data collected at 1.85, 1.00, 0.65, 0.5, 0.2M, 0.1, and 0.05 mM protein concentrations, respectively. Thus, to accurately evaluate the internal dynamics of OMP, it was very important that data be collected using cryogenic probe heads at low OMP concentrations ( $\leq 0.1 \text{ mM}$ ) where protein concentration had no effect on

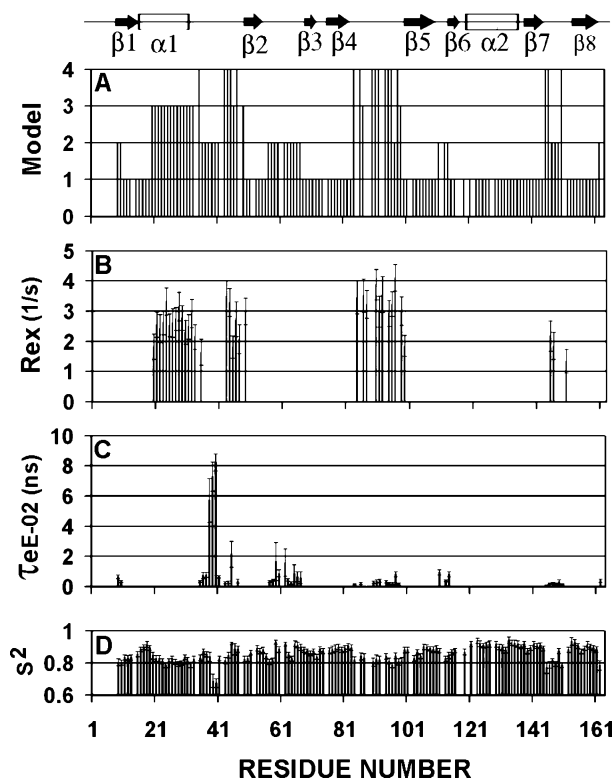


FIGURE 4: Histograms illustrating the model number and internal mobility parameters  $\tau_e$ ,  $R_{\text{ex}}$ , and  $S^2$  calculated for residues of OMP. These calculations used data from two magnetic fields (61 and 81 MHz) and assumed axially symmetric diffusion. The  $R_{\text{ex}}$  values are from data at 61 MHz.

$T_2$ . Additionally, a small degree of rotational anisotropy of the OMP was detected, which was modeled best by an axially symmetric diffusion tensor. The use of the solution and the crystal structure coordinates gave similar values in the optimization of the diffusion tensor parameters, and the calculated global  $\tau_m$  was identical ( $\tau_m = 8.93 \text{ ns}$ ).

Interestingly, similar internal mobility parameters, as obtained from the model-free analysis, are found to cluster in various defined sections of the protein's three-dimensional structure (Figures 4 and 5). For example, all residues comprising the core of the protein were characterized by high values of  $S^2$  and lack of internal motion contributions, and lower order parameters were observed for residues in the amino and carboxy termini as one might expect. Likewise, lower order parameters were consistent with the low  $^{15}\text{N}$ – $\{^1\text{H}\}$  NOE values found for residues in the loops of OMP and confirm flexibility for all three loops on the picosecond to nanosecond time scale.

Consistent with a well-defined  $\alpha 1$  helix in the NMR structure of OMP is the restricted motion on the picosecond to nanosecond time scale as revealed by a generalized order parameter,  $S^2$ , of  $0.83 \pm 0.02$ , on the average, for this helix. However, a significant contribution of motions on the millisecond time scale accounts for a substantial degree of conformational flexibility on slower time scales and can help to explain the lack of tertiary contacts in the original NMR structure (i.e., only four long-range constraints are reported in these regions). That this helix is not well packed into the rest of the protein could allow residues in this helix to come into and out of the helical secondary structure, which could

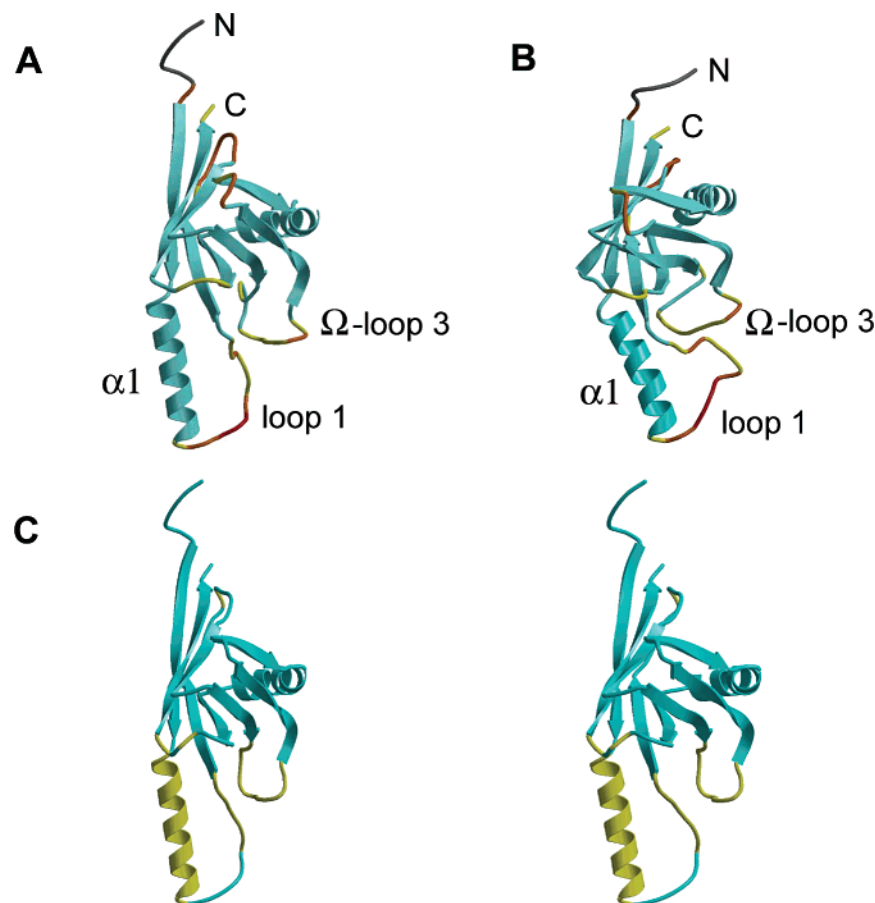


FIGURE 5: Ribbon diagrams of OMP illustrating the dynamic properties of OMP on fast and slow time scales. Ribbon diagrams of (A) the refined NMR and (B) the X-ray structures of OMP with a color gradient represent various degrees of mobility on fast time scales with colors ranging from sky blue to cyan for average order parameters,  $S^2$ , of  $0.88 \pm 0.02$  and  $0.82 \pm 0.02$ , respectively, and  $\tau_e = \tau_r < 20$  ps for both colors. For residues with higher degrees of motion, a color gradient from yellow to orange to red is used and represents residues with order parameters from  $S^2 < 0.75$  to  $S^2 = 0.65$  and  $\tau_r$  values from 20 to 825 ps. Residues with overlapping or weak correlation peaks (1–8 and 163) are shown in gray. (C) Stereoview of OMP with residues exhibiting motions on a slower time scale ( $R_{ex} > 1 \text{ s}^{-1}$ ) colored in yellow.

explain the uniformity in the  $R_{ex}$  values and the fast amide–proton exchange rates observed previously for residues in this helix (11). One may also speculate that helix 1 interacts with nearby loops, which are also displaying  $R_{ex}$ , giving rise to slow conformational exchange contributions to  $T_2$ ; such interactions with these loops could possibly invoke a relatively uniform movement of helix 1.

Unlike helix 1, both fast motions on the picosecond to nanosecond time scale and conformational exchange contributions on the millisecond time scale characterize the motional behavior of residues in  $\Omega$  loop 3 and loop 1. While there is no direct evidence about the direction of this motion, the close proximity of the segments that are involved is most easily explained by a single set of structural transitions between perhaps different functional states at this particular site. The highest values of  $R_{ex}$  for the residues in loop 1 and  $\Omega$  loop 3 confirm that these two segments of the protein allow a large degree of conformational flexibility at that site and may promote protein–protein interactions.

The ability of OMP to engage in protein–protein interactions was demonstrated by its interaction with Bex protein on phage display, Bex co-immunoprecipitation (12), and by the ability of Bex peptide 50–75 to induce significant perturbations in chemical shift values in the NMR spectrum of OMP upon its titration (11). The site of this peptide–

protein interaction was primarily within the  $\beta$ -clam cleft of OMP with half of the residues that exhibit the largest average chemical shift changes (E110, A114, D116, W117, N118, E119, A122) falling in the region between  $\Omega$  loop 3 and helix  $\alpha 2$ . Possibly the interaction of OMP with the full-length Bex protein would involve helix 2 and/or the loops of OMP (loops 1, 2, and 3) and helix 1 that have these dynamic properties.

## SUPPORTING INFORMATION AVAILABLE

Included are the experimental  $^{15}\text{N}$  relaxation rates,  $R_1$  and  $R_2$ , and  $^{15}\text{N}$ – $\{^1\text{H}\}$  NOE for OMP at 61 and 81 MHz  $^{15}\text{N}$  frequencies (Table 1s) and backbone internal motion parameters for OMP using coordinates from the NMR and X-ray structures (Table 2s). This material is available free of charge via the Internet at <http://pubs.acs.org>.

## REFERENCES

1. Margolis, F. L. (1980) A marker protein for the olfactory chemoreceptor neuron, in *Proteins of the Nervous System*, Raven Press, New York.
2. Margolis, F. L. (1988) Molecular cloning of olfactory specific gene products, in *Molecular Neurobiology of the Olfactory System*, Plenum Press, New York.
3. Buiakova, O. I., Baker, H., Scott, J. W., Farbman, A., Kream, R., Grillo, M., Franzen, L., Richman, M., Davis, L. M., Abbondanzo,



- S., Stewart, C. L., and Margolis, F. L. (1996) Olfactory marker protein (OMP) gene deletion alters physiological activity of olfactory neurons, *Proc. Natl. Acad. Sci. U.S.A.* 93, 9858–9863.
4. Youngentob, S., and Margolis, F. L. (1999) OMP gene causes an elevation in behavioral threshold sensitivity, *Neuroreport* 10, 15–19.
5. Youngentob, S. L., Margolis, F. L., and Youngentob, L. M. (2001) OMP gene deletion results in an alteration in odorant quality perception, *Behav. Neurosci.* 115, 626–631.
6. Ivic, L., Pyrski, M., Margolis, J. W., Richards, L. J., Firestein, S., and Margolis, F. L. (2000) Adenoviral vectormediated rescue of the OMP-null mouse, *Nat. Neurosci.* 3, 1113–1120.
7. Youngentob, S. L., Kent, P. F., and Margolis, F. L. (2003) OMP gene deletion results in an alteration in odorant-induced mucosal activity patterns, *J. Neurophysiol.* 90, 3864–3873.
8. Youngentob, S. L., Pyrski, M., and Margolis, F. L. (2004) Adenoviral vector-mediated rescue of the OMP-null behavioral phenotype: enhancement of odorant threshold sensitivity, *Behav. Neurosci.* 118, 636–642.
9. Kwon, H. J., Leinders-Zufall, F., and Margolis, F. L. (2004) OMP is a modulator of  $\text{Ca}^{2+}$  clearance processes in mouse olfactory neurons (ORNs), *ACHemS* 26, 150.
10. Behrens, M., Margolis, J. W., and Margolis, F. L. (2003) Identification of members of the Bex gene family as olfactory marker protein (OMP) binding partners, *J. Neurochem.* 86, 1289–1296.
11. Baldisseri, D. M., Margolis, J. W., Weber, D. J., and Margolis, F. L. (2002) Olfactory marker protein (OMP) exhibits a  $\beta$ -clam fold in solution: implications for target peptide interaction and olfactory signal transduction, *J. Mol. Biol.* 319, 823–837.
12. Koo, J. H., Gill, S., Pannell, L., Menco, B., and Margolis, F. L. (2004) The interaction of Bex and OMP reveals a metabolically active covalent dimer of OMP, *J. Neurochem.* 90, 102–116.
13. Smith, P. C., Firestein, S., and Hunt, J. F. (2002) The crystal structure of the olfactory marker protein at 2.3 Å resolution, *J. Mol. Biol.* 319, 808–821.
14. Chou, J. J., Gaemers, S., Howder, B., Louis, J. M., and Bax, A. (2001) A simple apparatus for generating stretched polyacrylamide gels, yielding uniform alignment of proteins and detergent micelles, *J. Biomol. NMR* 21, 377–382.
15. Chou, J. J., Kaufman, J. D., Stahl, S. J., Wingfield, P. T., and Bax, A. (2002) Micelle-induced curvature in a water-insoluble HIV-1 Env peptide revealed by NMR dipolar coupling measurement in stretched polyacrylamide gel, *J. Am. Chem. Soc.* 124, 2450–2451.
16. Ottiger, M., Delaglio, F., and Bax, A. (1998) Measurement of J and dipolar couplings from simplified two-dimensional NMR spectra, *J. Magn. Reson.* 131, 373–378.
17. Grzesiek, S., and Bax, A. (1993) The importance of not saturating  $\text{H}_2\text{O}$  in protein NMR: Application to sensitivity enhancement and NOE measurements, *J. Am. Chem. Soc.* 115, 12593–12594.
18. Piotto, M., Saudek, V., and Sklenar, V. (1992) Gradient-tailored excitation for signal-quantum NMR spectroscopy of aqueous solutions, *J. Biomol. NMR* 2, 661–665.
19. Kay, L. E., Nicolson, L. K., Delaglio, F., and Bax, A. (1992) Pulse Sequences for removal of the effects of cross correlation between dipolar and chemical shift anisotropy relaxation mechanisms on the measurement of heteronuclear  $T_1$  and  $T_2$  values in proteins, *J. Magn. Reson.* 97, 359–375.
20. Farrow, N. A., Muhandiram, R., Singer, A. U., Pascal, S. M., Kay, C. M., Gish, G., Shoelson, S. E., Pawson, T., Forman-Kay, J. D., and Kay, L. (1994) Backbone dynamics of a free and a phosphopeptide-complexed Src homology 2 domain studied by  $^{15}\text{N}$  NMR relaxation, *Biochemistry* 33, 5984–6003.
21. Sklenar, V., Torchia, D. A., and Bax, A. (1987) Measurement of carbon-13 longitudinal relaxation using  $^1\text{H}$  detection, *J. Magn. Reson.* 73, 375–379.
22. Delaglio, F., Grzesiek, S., Vuister, G. W., Zhu, G., Pfeifer, J., and Bax, A. (1995) NMRPipe: A multidimensional spectral processing system based on UNIX pipes, *J. Biomol. NMR* 6, 277–293.
23. Johnson, B. A., and Blevins, R. A. (1994) NMRview: a computer program for the visualization and analysis for NMR data, *J. Biomol. NMR* 4, 603–614.
24. Palmer, A. G., III, Rance, M., and Wright, P. E. (1991) Intramolecular motions of a zinc finger DNA-binding domain from xfn characterized by proton-detected natural abundance  $^{13}\text{C}$  heteronuclear NMR spectroscopy, *J. Am. Chem. Soc.* 113, 4371–4380.
25. Skelton, N. J., Palmer, A. G., III, Akke, M., Kordel, J., Rance, M., and Chazin, W. J. (1993) Practical aspects of two-dimensional proton-detected  $^{15}\text{N}$  relaxation measurements, *J. Magn. Reson., Ser. B* 102, 253–264.
26. Tjandra, N., Kuboniwa, N. H., Ren, H., and Bax, A. (1995) Rotational dynamics of calcium-free calmodulin studied by  $^{15}\text{N}$ -NMR relaxation measurements, *Eur. J. Biochem.* 230, 1014–1024.
27. Woessner, D. E. (1962) Nuclear spin relaxation in ellipsoids undergoing rotational Brownian motion, *J. Chem. Phys.* 37, 647–654.
28. Brüschweiler, R., Liao, X., and Wright, P. E. (1995) Long-range motional restrictions in a multidomain zinc-finger protein from anisotropic tumbling, *Science* 268, 886–889.
29. Kay, L. E., Torchia, D. A., and Bax, A. (1989) Backbone dynamics of proteins as studied by  $^{15}\text{N}$  inverse detected heteronuclear NMR spectroscopy: application to staphylococcal nuclease, *Biochemistry* 28, 8972–8979.
30. Tjandra, N., Feller, S. E., Pastor, R. W., and Bax, A. (1995) Rotational diffusion anisotropy of human ubiquitin from  $^{15}\text{N}$  NMR relaxation, *J. Am. Chem. Soc.* 117, 12562–12566.
31. Dosset, P., Hus, J. C., Blackledge, M., and Marion, D. (2000) Efficient analysis of macromolecular rotational diffusion from heteronuclear relaxation data, *J. Biomol. NMR* 16, 23–28.
32. Tillet, M. L., Blackledge, M. J., Derrick, J. P., Lian, L. Y., and Norwood, T. J. (2000) Overall rotational diffusion and internal mobility in domain II of protein G from *Streptococcus* determined from  $^{15}\text{N}$  relaxation data, *Protein Sci.* 9, 1210–1216.
33. de Alba, E., Baber, J. L., and Tjandra, N. (1999) The use of residual dipolar coupling in concert with backbone relaxation rates to identify conformational exchange by NMR, *J. Am. Chem. Soc.* 121, 4282–4283.
34. Cole, R., and Loria, J. P. (2003) FAST-Modelfree: A program for rapid automated analysis of solution NMR spin-relaxation data, *J. Biomol. NMR* 26, 203–213.
35. Mandel, A. M., Akke, M., and Palmer, A. G., III (1995) Backbone dynamics of *Escherichia coli* ribonuclease HI: correlations with structure and function in an active enzyme, *J. Mol. Biol.* 246, 144–163.
36. Blackledge, M., Cordier, F., Dosset, P., and Marion, D. (1998) Precision and uncertainty in the characterization of anisotropic rotational diffusion by  $^{15}\text{N}$  relaxation, *J. Am. Chem. Soc.* 120, 4538–4539.

BI050149T